Thermodynamic assessment of the LiF-BaF2-ZrF4 system

Dumaire, Thomas; Groot, Luuk; Schakenraad, Nynke M.; Beneš, Ondrej; Konings, Rudy J.M.; Smith, Anna L.

Important note
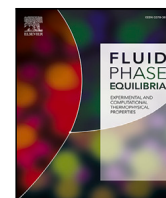To cite this publication, please use the final published version (if applicable).
Please check the document version above.

Thermodynamic assessment of the LiF–BaF$_2$–ZrF$_4$ system

Thomas Dumaire [a,b], Luuk Groot [a], Nynke M. Schakenraad [a], Ondrej Beneš [b], Rudy J.M. Konings [a,b], Anna L. Smith [a,*]

[a] *Delft University of Technology, Faculty of Applied Sciences, Radiation Science & Technology Department, Mekelweg 15, 2629 JB Delft, The Netherlands*
[b] *European Commission, Joint Research Centre (JRC), P.O. Box 2340, 76125 Karlsruhe, Germany*

ARTICLE INFO

ABSTRACT

Lithium-based fluoride salts are one of the leading options as fuel matrix in Molten Salt Reactors. The understanding of their thermodynamic behavior, e.g. chemical stability, activity, as well as heat transfer properties, in the reactor's environment is crucial for the safety assessment. In this work, the chemical equilibria of lithium fluoride with two important fission products dissolved in the salt matrix, namely barium fluoride and zirconium fluoride, are considered. The phase diagrams of the binary systems LiF–BaF$_2$, LiF–ZrF$_4$ and BaF$_2$–ZrF$_4$, as well as the ternary system LiF–BaF$_2$–ZrF$_4$ are assessed by the CALPHAD (CALculation of PHase Diagram) method using the quasichemical model in the quadruplet approximation for the liquid solution. These models are based on literature and new experimental data, and provide a good overview of the stability of intermediate compounds formed in the various systems and of the liquid solution.

1. Introduction

Molten Salt Reactors (MSRs) offer a promising alternative to conventional nuclear power plants due to their potential for improved safety, fuel utilization, and waste management [1]. Lithium-based fluoride salts, for instance ^{7}LiF–ThF$_4$–UF$_4$(–UF$_3$) [2], or the so-called FLiNaK (LiF-NaF-KF: 46.5-11.5-42 mol%) salt with dissolved AnF$_4$(–AnF$_3$) (An = actinide) [3], are leading candidates for use as a coolant and fuel carrier in MSRs, and have been characterized quite extensively already [4,5]. The composition of the fuel salt changes continuously in the reactor core due to the fission process, introducing new species that can be dissolved, form metallic precipitates, or form gaseous species [6,7]. By contrast with the base fuel salt, the knowledge on the thermodynamic properties and phase equilibria of the fission products in equilibrium with the fuel salt in the fuel salt is still limited, although information on irradiated fuel salt behavior is key for the design and optimization of MSRs.

Understanding the thermodynamics and phase behavior of the salt mixture in general is crucial for the safe and efficient operation of the new generation of molten salt reactors. The phase diagram of the salt mixture can be used to predict the formation of different phases, such as solid precipitates or gas phases, which can have a significant impact on the performance of the reactor. The thermodynamic modeling of the complex irradiated salt system allows to identify potential issues, such as corrosion or clogging related to metallic precipitates formation, and is a perfect tool to develop strategies to minimize their impact. It can

allow to anticipate equilibria in a complex fluid and to assess the risk of environmental impact in the event of accidental release.

As LiF is the main component of the fuel, it is essential to know how it interacts with the different compounds encountered in the reactor. Phase equilibria with actinides, such as ThF$_4$, UF$_4$ and PuF$_3$, composing the fresh fuels, have received particular attention in the literature [3,8,9]. Nowadays, the evolution of the fuel salt's composition and the possible change of its properties as a function of the burnup (residence time), with the addition of fission products [10], and corrosion products [11,12], is an important milestone to assess the safety of the MSR technology.

Barium is a major fission product that is produced during the nuclear power generation process. It is a highly reactive element that can potentially form compounds with other chemical elements from the fuel salt leading to a complex fuel chemistry. Zirconium is also a main fission product which can significantly contribute to the source term in an accidental scenario with release to the environment. ZrF$_4$ is particularly volatile in the liquid state and can easily vaporize. Furthermore, when zirconium dissolves in the fluoride matrix [6,13], it can also associate with other fission products, leading to the formation of multiple stable solid intermediate compounds, in association with for instance barium.

The most comprehensive experimental exploration of molten salt-fueled reactors in operation was carried out at the Oak Ridge National Laboratory, during the MSRE (Molten Salt Reactor Experiment). According to their measurements on various samples taken from a fully

---

Table 1
Purity and providers of the chemicals used in this work.

Compound	Provider	Purity
LiF powder	Alfa Aesar	99.99% (metal basis)
BaF$_2$ powder	Alfa Aesar	99.998% (metal basis)
ZrF$_4$ powder	Alfa Aesar	99.9% (metal basis)

operating (up to 9000 h) lithium-fueled reactor with ^{235}U, fission yields for the isotope ^{140}Ba were 5.43% and 6.01% for ^{95}Zr, respectively [14]. Based on their empirical observations, BaF$_2$ and ZrF$_4$ stable were soluble and were not removed during fuel reprocessing. Their presence in the salt matrix did not appear to interfere with the fission reaction. However, the dissolution of barium and zirconium in the fuel salt will affect its properties, and the formation of barium and zirconium compounds could become problematic if this occurs during reactor operation. These radioisotopes could also contribute to the release of harmful radioactive material into the environment in an accidental scenario [15]. Knowing how these fission products behave in the reactor core is therefore crucial for the safety assessment.

In this work, the experimental phase diagram data on the binary system LiF−BaF$_2$ were updated to resolve discrepancies found in the literature. Then, phase diagrams of LiF−BaF$_2$, LiF−ZrF$_4$ and BaF$_2$−ZrF$_4$ were modeled using the quasichemical model in the quadruplet approximation for the liquid solution, based on collected and literature data. Finally the assessments of the binaries were used to extrapolate and optimize the ternary system LiF−BaF$_2$−ZrF$_4$ based on mixing enthalpy data from the literature.

2. Experimental methods

2.1. Sample preparation

All experiments were performed in a glovebox with argon atmosphere, where O$_2$ and H$_2$O levels were maintained below 5 ppm. The starting materials were provided by Alfa Aesar: lithium (1+) fluoride LiF (99.99%), barium (2+) difluoride BaF$_2$ (99.998%) and zirconium (4+) tetrafluoride ZrF$_4$ (99.9%) (see Table 1). The powders were preliminary dried for 8 h at 500 K under argon atmosphere.

LiBaF$_3$ was the only intermediate compound synthesized in this work. The synthesis was done by the solid state method from a stoichiometric mixture of LiF and BaF$_2$ powders. The pure end-members were thoroughly blended in an agate mortar, and placed in a hermetically closed stainless steel container inside a nickel liner, then heated in a ceramic tubular furnace under argon flow for 8 h at 1093 K. The set heating and cooling rates were 5 K min^{-1} following the recommendation of Mishra et al. [16].

2.2. X-ray diffraction

The purity of the pure salts (e.g. LiF, BaF$_2$, ZrF$_4$) used as starting materials for the phase diagram measurements and synthesis of intermediate compounds, was checked using X-ray Diffraction (XRD) at room temperature (T = 293 ± 2 K), using a PANalytical X'Pert PRO X-ray diffractometer with a Cu anode (0.4 × 12 mm line focus, 45 kV, 40 mA). Samples were homogeneously distributed on a sample holder, closed under argon atmosphere with a Kapton® foil. X-ray data were collected by step scanning in the range 10° < 2θ < 120° in a Bragg–Brentano configuration. The X-ray scattered intensities were measured with a Real Time Multi Strip (RTMS) detector (X'Celerator). The purities of each powder salt was analyzed by Rietveld refinement method using the FullProf suite software [17,18], and no secondary phases were detected.

2.3. Differential scanning calorimetry

3D-heat flow measurements were conducted on the Setaram Multi Detector HTC module of the 96 line calorimeter. Every measurement

consisted of at least four consecutive heating cycles with 5 or 10 K min^{-1} heating rates and cooling rates of the same order. The transition temperature data were collected from the heat flow signals obtained on the heating ramps. All transition temperatures were extracted from the onset of the corresponding endothermic heat flow signal, except for the liquidus transition temperature that was taken from the maximum of the corresponding peak according to the NIST recommendations [19]. A correction was applied on the collected temperature data using a calibration equation determined with pure metals (In, Pb, Al, Ag, Au), to correct for the effects of the heating rate and apparatus geometry. The uncertainties on the reported temperatures is estimated ±5 K for pure compounds, and ±10 K for mixtures. The data collected in this work for the LiF−BaF$_2$, LiF−ZrF$_4$ and LiF−BaF$_2$−ZrF$_4$ systems are listed in Table 6 and in the corresponding phase diagram figures.

For the DSC measurements, the samples were prepared from the end-member powders, intimately mixed at the desired molar composition and inserted inside a pure nickel liner. The liners were hermetically closed in a stainless steel encasing designed according to the concept developed at the Joint Research Centre - Karlsruhe [20], limiting the vapor releases during the heating.

3. Thermodynamic modeling

The thermodynamic models reported herein were developed using the FactSage software version 8.2 [21], and are based on the CALPHAD (CALculation of PHAse Diagrams) method [22,23]. The optimization of the different parameters of the Gibbs energy functions for all phases present in the systems was based on available phase diagram and mixing enthalpy data. These were collected from different experimental studies [24–30], and in this work, and were correlated with the computed phase diagrams.

3.1. Gibbs energies of pure compounds

The Gibbs energy of pure compounds is expressed by:

$$G(\mathrm{T}) = \Delta_f H_m^o(298.15) - S_m^o(298.15)\cdot\mathrm{T} + \int_{298.15}^{\mathrm{T}} C_{p,m}(\mathrm{T})d\mathrm{T} - \mathrm{T}\int_{298.15}^{\mathrm{T}} \frac{C_{p,m}}{\mathrm{T}}d\mathrm{T} \tag{1}$$

where $\Delta_f H_m^o(298.15)$ is the standard enthalpy of formation, and $S_m^o(298.15)$ is the standard entropy of the pure compound at standard pressure and reference temperature 298.15 K. $C_{p,m}$ is the heat capacity expressed as a function of the temperature T.

3.2. Selected thermodynamic data

Thermodynamic data for lithium fluoride were taken from the Joint Research Centre Molten Salt Database (JRCMSD) which are taken from the NIST-JANAF recommendation [5,31,32]. The latter was also the source for BaF$_2$ thermodynamic functions [5,33]. BaF$_2$ shows two phase transitions before melting. The transition between the α phase and the β phase at T = 1240 K is reported to be a second order transition, while the transition from the β phase to the γ phase at T = 1480 K is of first order. The thermodynamic functions for ZrF$_4$ were taken from the SGTE database [34]. Several intermediate phases were reported in the literature for the binary LiF-BaF$_2$, LiF-ZrF$_4$, and BaF$_2$-ZrF$_4$ systems. The known and confirmed stoichiometries and crystal structures are listed in Table 2. For the intermediate compounds selected in this work for the modeling, the thermodynamic properties (enthalpy of formation, standard entropy and heat capacity) were not reported in existing literature. Therefore, the Neumann–Kopp rule was used to estimate the heat capacities [35]. Enthalpies of formation and standard entropies were first approximated from the stoichiometric sum of the pure end-member compounds, and then optimized during the modeling to fit the available phase diagram data. The optimized entropies were kept close

Table 2
Reported intermediate compounds and crystal structures in the LiF-BaF$_2$-ZrF$_4$ system. Note that high pressure phases have not been included.

Compound	Crystal symmetry	Space group	Reference
LiBaF$_3$	Cubic	$Pm\bar{3}m$ (221)	[36]
Li$_2$ZrF$_6$	Trigonal	$P\bar{3}1m$ (162)	[37]
Li$_4$ZrF$_8$	Orthorhombic	$Pnma$ (62)	[38]
Li$_3$Zr$_4$F$_{19}$	Triclinic	$P\bar{1}$ (2)	[38]
Ba$_3$ZrF$_{10}$	Orthorhombic	$Cmcm$ (63)	[39]
Ba$_2$ZrF$_8$	Orthorhombic	$Pnma$ (62)	[40]
α-BaZrF$_6$	Monoclinic	$P2_1/c$ (14)	[41]
β-BaZrF$_6$	Orthorhombic	$Cmme$ (67)	[42]
α-BaZr$_2$F$_{10}$	Monoclinic	$P\bar{1}$ (2)	[43]
β-BaZr$_2$F$_{10}$	Monoclinic	$C2/c$ (15)	[44]

to the additive approximation, since the entropies of formation of the intermediates compounds from the end-members (LiF, BaF$_2$ and ZrF$_4$) are expected to be relatively small.

The thermodynamic data of all compounds used and optimized in this work are listed in Table 3.

3.3. Solid solution modeling

A solid solution was observed in the BaF$_2$ − ZrF$_4$ system between the compositions X(ZrF$_4$) = 0.35 and X(ZrF$_4$) = 0.375 (Fig. 6). Defined as Ba$_{2+x}$Zr$_{1-x}$F$_{8+2x}$, this intermediate compound with homogeneity range was identified by Ratnikova et al. [46] and then by Grande et al. [29], as detailed below in Section 4.3. The existence of this solid solution was finally experimentally confirmed by Babitsyna et al. using a water-quenching melt method [47,48]. A one lattice polynomial model was used to describe the solid solution with Ba$_2$ZrF$_8$ and BaZrF$_6$ end-members. The Gibbs energy function G(T) of the solid solution is described by the equation:

$$G(\text{T}) = (X_{\text{Ba}_2\text{ZrF}_8} \cdot G^o_{m,\text{Ba}_2\text{ZrF}_8} + X_{\text{BaZrF}_6} \cdot G^o_{m,\text{BaZrF}_6}) - T\Delta S^{ideal} + \Delta G^{xs}_m \quad (2)$$

with

$$\Delta S^{ideal} = -R(X_{\text{Ba}_2\text{ZrF}_8} \ln X_{\text{Ba}_2\text{ZrF}_8} + X_{\text{BaZrF}_6} \ln X_{\text{BaZrF}_6}) \quad (3)$$

where $G^0_{m,\text{Ba}_2\text{ZrF}_8}$ and G^0_{m,BaZrF_6} are the molar Gibbs energies of the pure end-members with Ba$_2$ZrF$_8$ and BaZrF$_6$ stoichiometries, respectively, $X_{\text{Ba}_2\text{ZrF}_8}$ and X_{BaZrF_6} the molar fractions of the end-members, R the universal gas constant and ΔG^{xs} is the excess Gibbs energy. The excess Gibbs energy is expressed by:

$$\Delta G^{xs}_m = \sum_{i,j} X^i_A \cdot X^j_B \cdot q^{i,j} \quad (4)$$

where A and B represent Ba$_2$ZrF$_8$ and BaZrF$_6$, respectively, and $q_{i,j}$ is an interaction coefficient which can depend on temperature T described by the equation:

$$q^{i,j}_{A,B} = \alpha + \beta \, \text{T} \quad (5)$$

The optimized excess energy parameters are given by the following equation:

$$G^{xs}_{(\text{Ba}_2\text{ZrF}_8,\text{BaZrF}_6)} = X_{\text{Ba}_2\text{ZrF}_8} \cdot X_{\text{BaZrF}_6} \cdot 2000 \quad \text{J mol}^{-1} \quad (6)$$

In addition, to allow the formation of a solid solution around the Ba$_2$ZrF$_8$ composition in the phase diagram that does not extend fully towards BaZrF$_6$, the Gibbs energy of the BaZrF$_6$ end-member of the solid solution had to be destabilized according to:

$$G_{\text{BaZrF}_6}(ss) = G_{\text{BaZrF6}} + 4000 \quad \text{J mol}^{-1} \quad (7)$$

3.4. Liquid solutions modeling for binary systems

The liquid solutions were described by the modified quasichemical model in the quadruplet approximation [49,50], where the quadruplet

could be represented as two anions and two cations symmetrically disposed around an axis. Two atomic interactions are considered, the First Nearest Neighbor (FNN) interaction which describes the interaction cation–anion, and the Second Nearest Neighbor (SNN) interaction which describes the interactions between the two closest ions in the same sublattice. This model, which is particularly well-adapted to describe ionic liquids, allows to choose the composition of maximum short-range ordering in a binary system thanks to the variation of the ratio between the cation–cation coordination numbers $Z^A_{AB/FF}$ and $Z^B_{AB/FF}$. The short-range ordering is defined by the quadruplet approximation and includes the SNN interactions between each cation and each anion.

In a simple representation where A and B are two cations and F, the anion, the following reaction is obtained:

$$(A - F - A) + (B - F - B) \longrightarrow 2(A - F - B) \quad \Delta g_{AB/F} \quad (8)$$
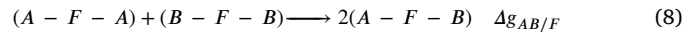
where $\Delta g_{AB/F}$ is the parameter of the Gibbs energy change associated with the SNN exchange reaction described as:

$$\Delta g_{AB/F} = \Delta g^0_{AB/F} + \sum_{i \geq 1} g^{i0}_{AB/F} \chi^i_{AB/F} + \sum_{j \geq 1} g^{0j}_{AB/F} \chi^j_{BA/F} \quad (9)$$

where $\Delta g^0_{AB/F}$ and $g^{ij}_{AB/F}$ are possibly dependent on temperature, but independent of composition, and optimized to fit as best as possible the experimental data available on a given system. The dependence on composition is given by the term $\chi_{AB/F}$ defined as:

$$\chi_{AB/F} = \frac{X_{AA}}{X_{AA} + X_{AB} + X_{BB}} \quad (10)$$

where X_{AA}, X_{AB} and X_{BB} represent the different cation–cation pair fractions. To maintain electro-neutrality in the system, the anion–anion coordination should be determined. The following equation is applied after the selection of cation–cation coordination numbers:

$$\frac{q_A}{Z^A_{AB/FF}} + \frac{q_B}{Z^B_{AB/FF}} = 2 \cdot \frac{q_F}{Z^F_{AB/FF}} \quad (11)$$

with q_i representing the charges of the different ions and $Z^F_{AB/FF}$ is the anion–anion coordination number. These choices are based on the optimization of the systems in order to get the maximum short range ordering and highest excess Gibbs energy at a composition usually around the lowest eutectic in the phase diagram. The coordination numbers selected in this work are listed in Table 4.

The optimized excess Gibbs energy of the liquid solutions obtained during the modeling of the binary systems determined in this work are given by the following equations:

$$\Delta g_{\text{LiBa}/FF} = -1900 + 2 \, \text{T} - 1500\chi_{\text{LiBa}/FF} + (-6500 + 4.3 \, \text{T})\chi_{\text{BaLi}/FF} \quad \text{J mol}^{-1} \quad (12)$$

$$\Delta g_{\text{LiZr}/FF} = -26000 + 3 \, \text{T} + (-5500 + 2.2 \, \text{T})\chi_{\text{LiZr}/FF}$$
$$+ (-22000 - 4.9 \, \text{T})\chi_{\text{ZrLi}/FF} + (7000 + 23 \, \text{T})\chi^2_{\text{ZrLi}/FF} \quad \text{J mol}^{-1} \quad (13)$$

$$\Delta g_{\text{BaZr}/FF} = -30400 - (25000 + 15 \, \text{T})\chi_{\text{ZrBa}/FF} + 3000\chi^2_{\text{BaZr}/FF} \quad \text{J mol}^{-1} \quad (14)$$

3.5. Liquid solution for the ternary system

For the LiF − BaF$_2$ − ZrF$_4$ system, the ternary diagram was modeled from the binary sub-systems LiF − BaF$_2$, LiF − ZrF$_4$ and BaF$_2$ − ZrF$_4$ described above using the Kohler/Toop interpolation [51], where the latter is an asymmetric interpolation model of two groups of symmetry: the monovalent group of LiF considered as dissociated ionic liquid, and bivalent BaF$_2$ plus tetravalent ZrF$_4$ more likely to form molecular and oligomer species in the melt. Optimization of the ternary excess parameters was based on the only data available for the ternary system,

Table 3

Thermodynamic data for end-members and intermediate compound used in this work for the thermodynamic model. Standard enthalpy of formation $\Delta_f H_m^o$ (298.15 K), standard entropy S_m^0 (298.15 K) and heat capacity coefficient of pure compounds $C_{p,m}$ (T/K)/(J K^{-1} mol^{-1}) = a + b·T + c·T^2 + d·T^{-2}. Values optimized in this work in the thermodynamic modeling assessment are marked in bold.

Compound	$\Delta_f H_m^0$(298.15 K) (kJ mol^{-1})	S_m^0(298.15 K) (J K^{-1} mol^{-1})	$C_{p,m}$ (T/K)/(J K^{-1} mol^{-1}) = a + b·T + c·T^2 + d·T^{-2} a	b	c	d	T (K)	Ref.
LiF$_{(cr)}$	−616.931	35.66	43.30898	0.016312168	5.0470398·10^{-7}	−569123.6	298.15–2500	[33]
LiF$_{(l)}$	−598.654	42.96	64.183	–	–	–	298.15–6000	[33]
LiF$_{(g)}$	−340.946	200.08	35.397917	1.870664·10^{-3}	−1.654306·10^{-7}	–	298.15–6000	[33]
Li$_2$F$_{2(g)}$	−942.781	258.52	60.80524	5.13678·10^{-2}	−3.433579·10^{-5}	−882301	298.15–600	[33]
			82.55869	3.852765·10^{-4}	−6.715069·10^{-8}	−2142689	600–3100	[33]
			83.05533	2.587352·10^{-5}	−2.112209·10^{-9}	−2215248	3100–6000	[33]
Li$_3$F$_{3(g)}$	−1517.202	317.97	97.43992	8.075246·10^{-2}	−5.345478·10^{-5}	−1266154	298.15–600	[33]
			131.0814	1.723168·10^{-3}	−4.214711·10^{-7}	−3179819	600–2000	[33]
			132.9855	1.516407·10^{-5}	−1.454542·10^{-9}	−3852585	2000–6000	[33]
α-BaF$_{2(cr)}$	−1208.758	96.399	84.428	−0.0133132	1.872487·10^{-5}	−881.770	298.15–700	[33]
			510.809	−0.7551455	0.0003813337	−42423270	700–1100	[33]
			30 262.42	−36.20693	0.0122619	−6249891000	1100–1240	[33]
β-BaF$_{2(cr)}$[a]			444.9684	−0.236396	–	–	1240–1481	[33]
γ-BaF$_{2(cr)}$[b]			107.6543	–	–	–	1481–1641	[33]
BaF$_{2(l)}$	−1182.7251	112.440	99.82606	–	–	–	1641–3500	[33]
BaF$_{2(g)}$	−803.7464	301.186	57.28314	1.299299·10^{-3}	−4.94381·10^{-7}	−341665.4	298.15–1400	[33]
			58.20781	−2.102083·10^{-6}	1.858868·10^{-10}	−475260.6	1400–6000	[33]
ZrF$_{4(cr)}$	−1911.300	104.6	81.64412	0.08062462	−1.957282·10^{-5}	−21580.19	298.15–1183	[34,45]
ZrF$_{4(l)}$	−1850.300	156.16	150	–	–	–	1183–2000	[34,45]
ZrF$_{4(g)}$	−1669.506	322.77	93.77765	2.462543·10^{-2}	−1.198783·10^{-5}	−1112192	298.15–900	[34,45]
			107.9527	5.26574·10^{-5}	−5.370488·10^{-9}	−2544208	900–6000	[34,45]
LiBaF$_{3(cr)}$	**−1829.689**	**132.1**	**127.73698**	**0.002998968**	**1.872487·10^{-5}**	**−881770**	**298.15–6000**	This work (model)[c]
Li$_2$ZrF$_{6(cr)}$	**−3184.500**	**170.0**	**202.231**	**0.053124**	**1.01·10^{-6}**	**−2738757**	**298.15–2500**	this work (model)[c]
Li$_4$ZrF$_{8(cr)}$	**−4419.800**	**241.3**	**288.8489**	**0.085749**	**2.02·10^{-6}**	**−3877004**	**298.15–2500**	This work (model)[c]
Li$_3$Zr$_4$F$_{19(cr)}$	**−9558.500**	**515.0**	**592.3789**	**0.130937**	**1.51·10^{-6}**	**−8109411**	**298.15–2500**	This work (model)[c]
Li$_3$ZrF$_{7(cr)}$	**−3755.050**	**270.0**	**245.53994**	**0.069436504**	**1.51411·10^{-6}**	**−3307880.8**	**298.15–2500**	This work (model)[c]
α-BaZrF$_{6(cr)}$	**−3158.090**	**215.0**	**166.07212**	**0.06731142**	**−8.4795·10^{-7}**	**−903350.19**	**298.15–817.15**	This work (model)[c]
β-BaZrF$_{6(cr)}$	**−3153.090**	**215.0**	**166.07212**	**0.06731142**	**−8.4795·10^{-7}**	**−903350.19**	**298.15–817.15**	This work (model)[c]
Ba$_2$ZrF$_{8(cr)}$	**−4396.567**	**311.5**	**250.50012**	**0.05399822**	**1.787692·10^{-5}**	**−178120.19**	**298.15–6000**	This work (model)[c]
Ba$_3$ZrF$_{10(cr)}$	**−5635.500**	**392.5**	**334.92812**	**0.04068502**	**3.660179·10^{-5}**	**−2666890.19**	**298.15–6000**	This work (model)[c]
α-BaZr$_2$F$_{10(cr)}$	**−5056.700**	**345.0**	**247.71624**	**0.14793604**	**2.042077·10^{-5}**	**−924930.38**	**298.15–796.15**	This work (model)[c]
β-BaZr$_2$F$_{10(cr)}$	**−5053.700**	**345.0**	**247.71624**	**0.14793604**	**2.042077·10^{-5}**	**−924930.38**	**796.15–6000**	This work (model)[c]

[a] $\alpha \leftrightarrow \beta$ second order transition at 1240 K, $\Delta H_{tr}(T_{tr})$ = 0 kJ mol^{-1}.

[b] $\beta \leftrightarrow \gamma$ first order transition at 1480 K, $\Delta H_{tr}(T_{tr})$ = 2.6736 kJ mol^{-1}.

[c] Heat capacity obtained using the Neumann–Kopp approximation [35].

Table 4

Coordination numbers of the liquid solution used in this work.

A	B	$Z_{AB/FF}^A$	$Z_{AB/FF}^B$	$Z_{AB/FF}^F$
Li$^+$	Li$^+$	6	6	3
Ba^{2+}	Ba^{2+}	6	6	3
Zr^{4+}	Zr^{4+}	6	6	1.5
Li$^+$	Ba^{2+}	2	6	2.4
Li$^+$	Zr^{4+}	2	6	1.71
Ba^{2+}	Zr^{4+}	4	6	1.71

from Hatem et al. [30,52]. These authors measured the mixing enthalpy on different pseudobinary sections of the ternary system and were the base for the optimization (Section 4.4). More detail will be given in the next section. The ternary excess parameter optimized for the system LiF−BaF$_2$−ZrF$_4$ is given below:

$$\Delta g_{LiBa(Zr)/FF}^{011} = -90000 \quad \text{J mol}^{-1} \tag{15}$$

3.6. Gas phase

The gas phase is described by an ideal mixture of (LiF, Li$_2$F$_2$, Li$_3$F$_3$, BaF$_2$, and ZrF$_4$) gaseous species. The Gibbs energy is expressed by:

$$G^\varphi = \sum_i y_i \, ^oG_i^\varphi + RT \sum_i y_i ln y_i + RT ln P/P^o \tag{16}$$

where y_i is the fraction of the species i in the gas phase, $^oG_i^\varphi$ the standard Gibbs energy of the gaseous species i, and P^o the standard pressure. The functions for the gaseous species are listed in Table 3.

To the best of our knowledge, only vapour pressure studies in the LiF-ZrF$_4$ binary system have been reported in the literature [53,54]. Sense and Stone suggested the existence of the LiZr$_2$F$_9$ gaseous molecule above the LiF-ZrF$_4$ binary mixture. In the absence of structural and thermodynamic data for the latter species, it was not included in the present assessment. A comprehensive assessment of the vapour pressures in the LiF-BaF$_2$-ZrF$_4$ system is out of the scope of the present study, as it would require complementary experimental investigations.

4. Results and discussions

4.1. LiF−BaF$_2$

Phase diagram data were measured on this system by thermal analysis measurement techniques by Bergman and Banashek [24], Boukhalova [55], Taniuchi et al. [56], and Agulyanskii and Bessanova [25]. In the works of [24,25,55], the melting temperature of pure BaF$_2$ was measured at 1553 K, at odds with the temperature selected by the NIST-JANAF tables [33], (1641 ± 2) K (selected for the present assessment). The agreement between the four studies is generally good, as seen from Fig. 2, although the data of Boukhalova [55] and Agulyanskii and Bessanova [25] show some discrepancy with results obtained in this work and in the other two studies, and are thus considered less reliable. The data reported by Taniuchi et al. [56] and Bergman and Banashek [24] are consistent with respect to the eutectic transition temperature and composition. The experimental data measured in this work (Table 6), have enabled the determination of the peritectic decomposition temperature of LiBaF$_3$, and liquidus curve in
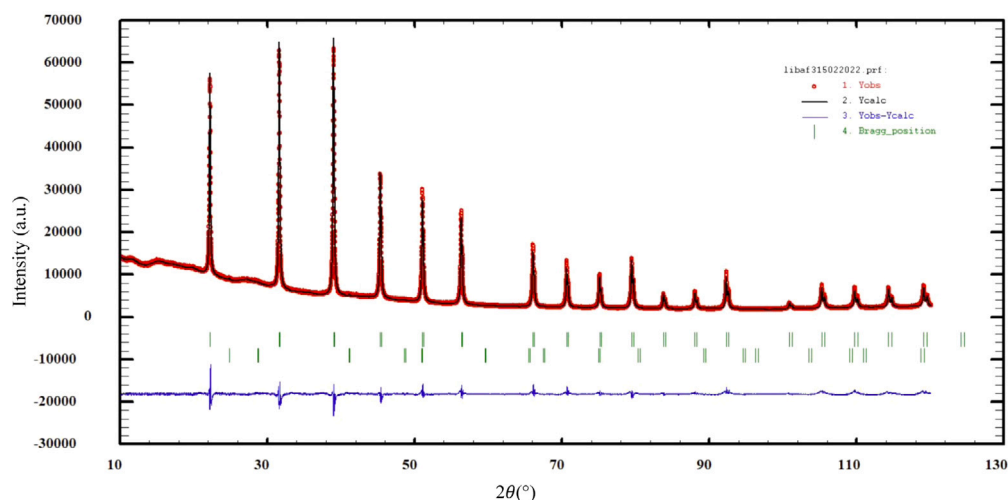
Fig. 1. Diffractogram of LiBaF$_3$ synthesized in this work Y$_{obs}$ (red dots), measured at (293 ± 2) K with Cu anode, compared to the Rietveld refinement performed on the FullProf suite software. Represented by: Y$_{calc}$ (black line) the calculated XRD pattern and Y$_{obs}$ - Y$_{calc}$ (blue line) the differential calculation between observed and calculated data. The Bragg's reflection angular positions of LiBaF$_3$ ((99.7 ± 0.2)%) (top) and BaF$_2$ ((0.3 ± 0.2)%) (bottom) are shown by green marks.
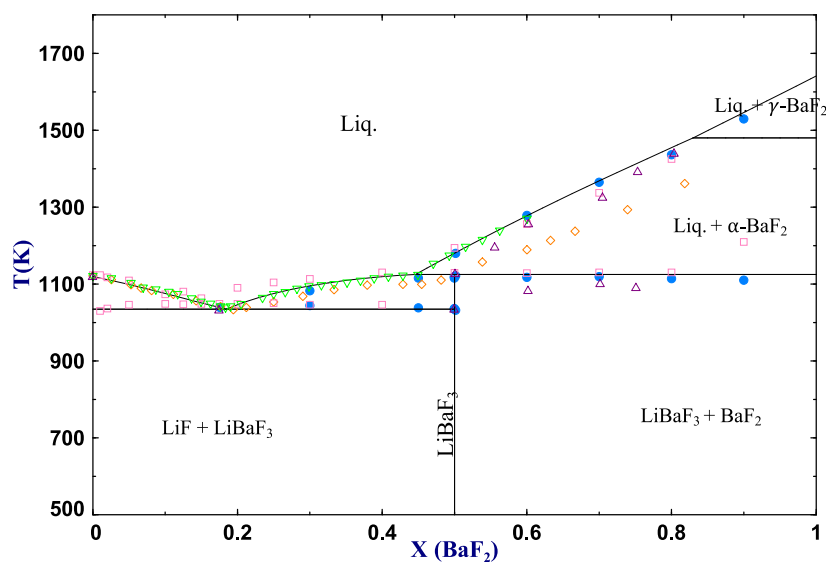
Fig. 2. Phase diagram of the LiF–BaF$_2$ system calculated in this work. (●) are the transitions measured experimentally in this work, (▽) represent the data from Bergman and Banashek [24], (◇) the data from Boukhalova [55], (△) the data from Taniuchi [56], and (□) the data from Agulyanskii and Bessanova [25].

greater detail at high BaF$_2$ concentrations (from X$_{(BaF_2)}$ = 0.6 to 1), with a trend that is consistent with the selected reference value for the melting temperature of the BaF$_2$ end-member. Although the melting temperature of pure BaF$_2$ could not be measured with the equipment used in this work, it is in line with the measured trend of the liquidus temperatures at high BaF$_2$ concentrations.

The peritectic decomposition at the stoichiometric composition LiBaF$_3$ was measured on the synthesized sample (see Section 2.1). The XRD measurement conducted on the sample confirmed a cubic antiperovskite (P$m3m$(221)) crystal structure [36] (see Table 2), and the product's purity was found to be (99.7 ± 0.2)% (with BaF$_2$ impurities) by Rietveld refinement (Fig. 1) [17]. The experimental results are listed in Table 6 and the invariant equilibria in the phase diagram are listed in Table 5.

Mixing enthalpy data were measured experimentally at T = 1354 K using twin micro-calorimetry by Hong and Kleppa [57]. From the calculation at the same temperature with the present model (Fig. 3), the agreement is confirmed with the experimental data and particularly with the extrapolation proposed by Kleppa et al.

The model proposed here (Fig. 2) reproduces well the new experimental data provided in this work. It is also conform to the invariant equilibria composition and temperature determined in the works of Bergman and Banashek [24], Boukhalova [55], Taniuchi et al. [56], and Agulyanskii and Bessanova [25], with the exception of the melting temperature of BaF$_2$ as explained above.

4.2. LiF–ZrF$_4$

A first set of phase diagram data were measured for the LiF–ZrF$_4$ system by Thoma et al. [27], who used different methods, namely quenching and differential scanning calorimetry. ZrF$_4$ is particularly volatile in solutions containing free F$^-$ anions [58,59], so measurements at high ZrF$_4$ content are particularly difficult. The reported data were collected during cooling of the samples, allowing to confirm the exact composition on quenched samples. The experimental procedures are presented in further detail in ORNL reports and publications from the same authors [60–62], including details on the experimental accuracies. The quenching method was privileged by Thoma to obtain

Table 5

Invariant equilibria calculated in this work for the system LiF−BaF$_2$ compared to the experimental data measured and the references provided in the literature.

Invariant Reaction	Equilibrium	Calculated and literature data					
		This study (model)		Agulanskii et al. [25]		Tanuichi et al. [56]	
		X$_{BaF_2}$	T (K)	X$_{BaF_2}$	T (K)	X$_{BaF_2}$	T (K)
LiF + LiBaF$_3$ = L	Eutectic	0.185	1034	0.175	1048	0.194	1033
LiBaF$_3$ = L′ + BaF$_2$	Peritectic transition	0.5	1123	0.5	1129	0.5	1110
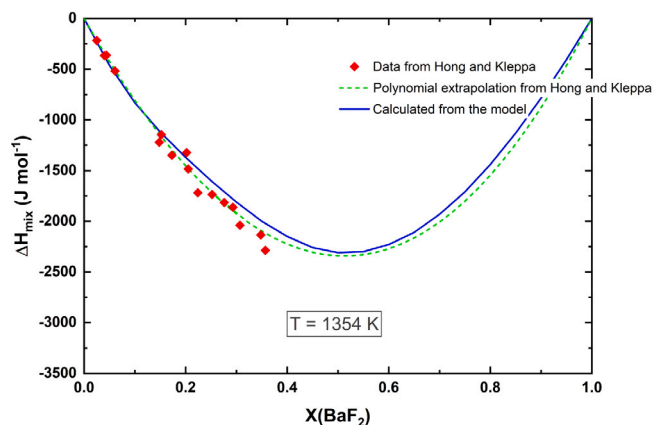
Fig. 3. Mixing enthalpy of the LiF−BaF$_2$ system calculated at 1354 K in this work, compared to the experimental data and polynomial fitting by Kleppa et Hong [57]. The calculation were performed with a constant pressure of 1 atm.

Table 6
DSC data collected in this work.

X$_{LiF}$	X$_{BaF_2}$	X$_{ZrF_4}$	T (K)	Equilibrium	Invariant reaction
–	1	–	1124	Congruent melting	LiF = L
0.824	0.176	–	1039	Eutectic	LiF+LiBaF$_3$ = L
0.700	0.300	–	1044	Eutectic	LiF+LiBaF$_3$ = L
0.700	0.300	–	1082	Liquidus	L′+LiBaF$_3$ = L
0.550	0.450	–	1038	Eutectic	LiF+LiBaF$_3$ = L
0.550	0.450	–	1115	Liquidus	L′+LiBaF$_3$ = L
0.500	0.500	–	1036	Eutectic	LiF+LiBaF$_3$ = L
0.500	0.500	–	1121	Peritectic	LiBaF$_3$ = L′+BaF$_2$
0.493	0.507	–	1119	Peritectic	LiBaF$_3$ = L′ +BaF$_2$
0.493	0.507	–	1180	Liquidus	L′+BaF$_2$ = L
0.400	0.600	–	1117	Peritectic	LiBaF$_3$ = L′ + BaF$_2$
0.400	0.600	–	1278	Liquidus	L′ + BaF$_2$ = L
0.300	0.700	–	1119	Peritectic	LiBaF$_3$ = L′+BaF$_2$
0.300	0.700	–	1364	Liquidus	L′ + BaF$_2$ = L
0.248	0.752	–	1114	Peritectic	LiBaF$_3$ = L′+BaF$_2$
0.248	0.752	–	1436	Liquidus	L′ + BaF$_2$ = L
0.111	0.889	–	1110	Peritectic	LiBaF$_3$ = L′+BaF$_2$
0.111	0.889	–	1529	Liquidus	L′ + BaF$_2$ = L
0.776	–	0.224	765	Peritectoid	Li$_2$ZrF$_6$ + Li$_4$ZrF$_8$ = Li$_3$ZrF$_7$
0.776	–	0.224	855	Eutectic	LiF + Li$_3$ZrF$_7$ = L
0.776	–	0.224	881	Liquidus	L′ + Li$_3$ZrF$_7$ = L

Uncertainty for the temperature measurements are estimated at ±5 K for pure compounds, and ±10 K for mixtures.

the experimental data on the liquidus transitions, while the differential calorimetry data on the cooling ramps were selected according to Thoma's recommendations for the solidus and crystalline transitions. A second complete set of phase diagram data is provided by Korenev et al. [63], who used differential thermal analysis and X-ray diffraction. The reported liquidus equilibria are very similar to the previous work. The only significant difference is that Korenev identified only one congruent melting for Li$_3$ZrF$_7$, while he suggested a peritectic decomposition for Li$_2$ZrF$_6$. On the ZrF$_4$-rich side, the authors also observed an $\alpha \rightarrow \beta$-ZrF$_4$ polymorphic transition. In a study on the crystal structures of the intermediates Li$_4$ZrF$_8$ and Li$_3$Zr$_4$F$_{19}$, Dugat et al. moreover re-investigated the LiF-ZrF$_4$ phase diagram [38]. The authors collected

experimental data for a few concentrations, but the invariant equilibria were not defined precisely. Considering more recent works on the crystal structure of ZrF$_4$ (it was showed that the β and γ phases are not stable above 673 K, and the γ-ZrF$_4$ was stabilized only for a high pressure of 28 GPa [64,65]), it was decided not to include any phase transition in ZrF$_4$ for the thermodynamic models.

The model shows overall a good agreement with the literature data and the invariant equilibria (Table 7). Only the liquidus temperatures around the congruently melting compound Li$_3$ZrF$_7$ are not reproduced as well as the rest of the data. It was not achievable to match the liquidus data in this region at the same time as the mixing enthalpy data and reported eutectic equilibria. We therefore attempted to re-measure the phase equilibria in this region. Our measurement at X$_{ZrF_4}$ = 0.224 yielded a slightly lower liquidus temperature than reported by Thomas et al. [27], and in better agreement with the optimization (Fig. 4). Obviously, the comprehensive re-examination of this composition range would be highly beneficial. The introduction of multiple coordination environments that could reflect better the local structure of the melt [9,66], where oligomerization is expected [67], could help reproduce this region of the phase diagram with a higher accuracy. It is finally worth pointing out that the gas in equilibrium with solid ZrF$_4$ reaches 1 bar at T = 1175 K (i.e., below its melting temperature), which is related to the low boiling point and high volatility of ZrF$_4$.

Using the current assessment, the mixing enthalpy calculated from the model shows good agreement with the trend of the experimental data from Hatem et al. [68] (see Fig. 5).

4.3. BaF$_2$−ZrF$_4$

In the literature, the phase diagram of the BaF$_2$−ZrF$_4$ system was studied by several groups. In 1989, Babitsyna et al. measured a first series of phase equilibria between X(ZrF$_4$) = 0.33 and X(ZrF$_4$) = 1 [47,48]. The authors reported four intermediate compounds, namely Ba$_2$ZrF$_6$, Ba$_3$Zr$_2$F$_{14}$, BaZrF$_6$ and BaZr$_2$F$_{10}$. The latter compound was reported with a peritectic decomposition at T = 850 K [48]. Ba$_2$ZrF$_8$ was defined with a stable homogeneity range and a congruent melting at T = 1285 K.

In 1992, Grande et al. [29], reported new results by thermal analysis and compared their results to the work by Babitsyna et al. [48]. They observed that the transition data previously collected by Babitsyna et al. for pure ZrF$_4$ were not reliable: they found a melting temperature at (1183 ± 1) K, in agreement with literature recommended by the SGTE and NIST-JANAF databases [33,34], in contrast with the previous work (1273 K). No phase transition was observed for pure BaF$_2$ [29]. A congruent melting was identified for BaZr$_2$F$_{10}$ at a temperature of (863 ± 2) K by thermal analysis. The latter transition was also reported around the same temperature by other authors [46–48], but defined as a crystalline transition. Congruent melting was found for Ba$_2$ZrF$_8$ at (1289 ±1) K. Two phase transitions were also identified, at 796 K and 813 K, respectively. These results were moreover confirmed by X-ray Diffraction of the different polymorphs in quenched samples. A last work, by Ratnikova et al. in 1997 [46], shows a phase diagram without BaZr$_2$F$_{10}$, but with an homogeneity range for Ba$_2$ZrF$_8$, melting congruently. The phase equilibria at high temperature of the BaF$_2$−ZrF$_4$ system were also studied by Lin et al. [69], particularly at high concentration of ZrF$_4$, where previous work gave inconsistent
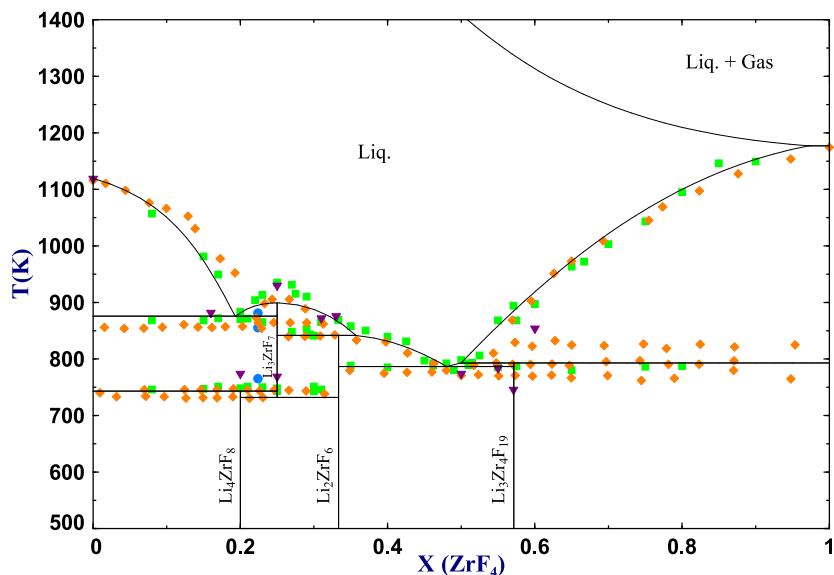
Fig. 4. Phase diagram of the $LiF-ZrF_4$ system calculated in this work. (●) are the transitions measured experimentally in this work, (■) represent the data from Thoma et al. [27], (◆) the data from Korenev et al. [63] and (▼) the data from Dugat et al. [38]. The calculation was performed for a constant pressure of 1 atm.

Table 7
Invariant equilibria calculated in this work for the system $LiF-ZrF_4$ compared to the references provided in the literature.

| Invariant Reaction	Equilibrium	Calculated and literature data					
		This study (model)		Thoma et al. [27]		Korenev et al. [63]	
		X_{ZrF_4}	T (K)	X_{ZrF_4}	T (K)	X_{ZrF_4}	T (K)
$LiF + Li_3ZrF_7 = L$	Eutectic	0.194	899	0.21	871 ± 2	0.21	858 ± 5
$Li_3ZrF_7 = L$	Congruent melting	0.250	886	0.25	935 ± 5	0.25	913 ± 5
$Li_2ZrF_6 + Li_4ZrF_8 = Li_3ZrF_7$	Peritectoid	0.250	731	0.25	743 ± 3	0.25	747 ± 5
$Li_2ZrF_6 = L' + Li_3ZrF_7$	Peritectic	0.333	842	0.295	843 ± 2	0.33	843 ± 5
$Li_2ZrF_6 + Li_3Zr_4F_{19} = L$	Eutectic	0.481	786	0.49	780 ± 3	0.50	775 ± 5
$Li_3Zr_4F_{19} = ZrF_4 + L'$	Peritectic	0.571	791	0.571	793 ± 5	*not identified*	
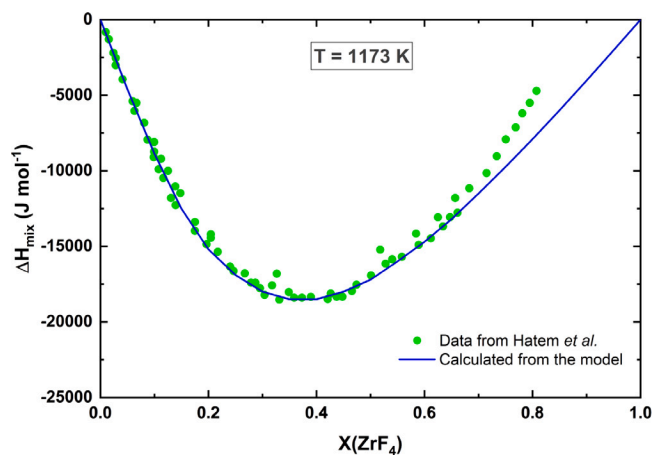
Fig. 5. Mixing enthalpy of the $LiF-ZrF_4$ system calculated at 1173 K in this work, compared with the experimental data from Hatem et al. [68].

data. The model proposed here (Fig. 6), is in good agreement with data by Grande et al. [29], selected as reference for the optimization because the information in the paper allows for a detailed evaluation of experimental methods and interpretation. A comparison with the other datasets allows to consider this model as a satisfactory representation of the system BaF_2-ZrF_4 overall (Table 8).

4.4. Ternary $LiF-BaF2-ZrF_4$

The optimization of the ternary phase diagram was based on the only set of experimental data determined by drop calorimetry and differential thermal analysis by Mahmoud [52], describing the mixing enthalpy along different pseudobinary sections (as defined in Fig. 7) of the phase diagram, shown in Figs. 8 and 9. No mutual solid solubility is expected in the ternary system in between the intermediate compounds stable in the binary systems as the stoichiometries and crystal structures differ from one system to the other. Moreover, the large difference in ionic radius between the Li^+ and Ba^{2+} cations makes it unlikely for such solid solutions to form. A quaternary compound was reported, however, in the ternary system, with stoichiometry $LiBaZr_2F_{11}$, and tetragonal symmetry in space group $I4/m$ [70]. The latter was prepared with a hydrothermal synthesis route at 180°C in an hermetic Teflon jar. The information provided by Gao et al. [70] in their study does not allow to conclude if $LiBaZr_2F_{11}$ is a stable phase under standard pressure. We could also not find any thermodynamic data for the latter compound in the literature. The melting/decomposition temperature is not known. In the absence of sufficient information, the quaternary phase $LiBaZr_2F_{11}$ was thus not included in the present thermodynamic assessment.

The ternary excess parameters of the liquid solution, obtained for a Kohler-Toop interpolation (X_{LiF} = asymmetric component) [71], allow a very good agreement in the different $(LiF/BaF_2)-ZrF_4$ sections (Fig. 8). These data were first used for the optimization, considering their lower uncertainty ($\pm 3\%$), compared to the sections $(LiF/ZrF_4)-BaF_2$ ($\pm 6\%$) [52]. However, even for the latter case, the model remains also in very good agreement with these other data (Fig. 9).
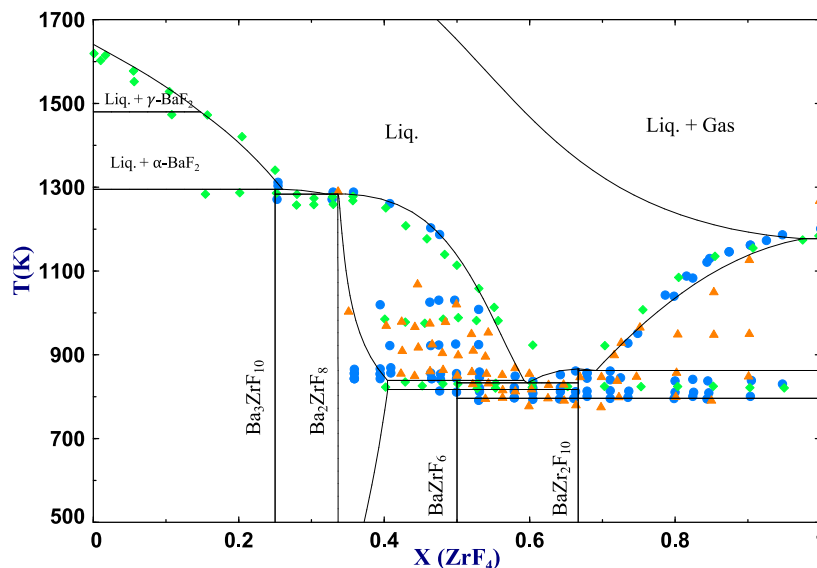
Fig. 6. Phase diagram of the BaF_2-ZrF_4 system calculated in this work. (●) are the data from Grande et al. [29], (◆) represent the data from Ratnikova et al. [46], and (▼) the data from Babitsyna et al. [47]. The calculation was performed for a constant pressure of 1 atm.

Table 8
Invariant equilibria calculated in this work for the system BaF_2-ZrF_4 compared to the references provided in the literature.

Invariant Reaction	Equilibrium	Calculated and literature data					
		This study (model)		Grande et al. [29]		Ratnikova et al. [46]	
		X_{ZrF_4}	T (K)	X_{ZrF_4}	T (K)	X_{ZrF_4} [a]	T (K)
$Ba_3ZrF_{10} = BaF_2 + L'$	Peritectic	0.250	1294	0.250	1305	0.29	1285
$Ba_3ZrF_{10} + Ba_2ZrF_8 = L$	Eutectic	0.321	1283	0.30	1270	0.31	1259
$Ba_2ZrF_8 = L$	Congruent melting	0.333	1283	0.336	1289	0.333	1279
β-$BaZrF_6 = Ba_2ZrF_8 + L'$	Peritectic	0.500	838	0.500	858	0.500	833
β-$BaZrF_6 + BaZr_2F_{10} = L$	Eutectic	0.597	832	0.62	822	*Only one eutectic*	
$BaZr_2F_{10} = L$	Congruent melting	0.667	866	0.667	863	*identified:*	
$BaZr_2F_{10} + ZrF_4 = L$	Eutectic	0.691	862	0.7	842	0.65	828

[a] Uncertainty on the composition reported to be: ± 0.02.

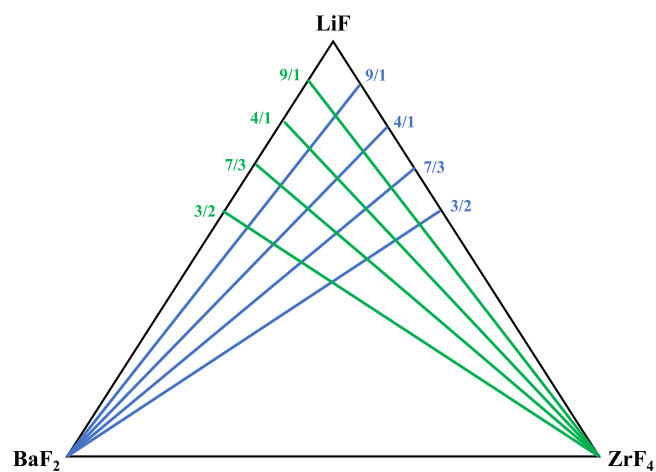**Fig. 7.** Pseudobinary sections experimentally assessed in the ternary system $LiF-BaF_2-ZrF_4$ at 1173 K measured by Mahmoud [52] and calculated in this work.

Although the ternary mixing enthalpy data do not cover the entire spectrum of composition in the ternary phase diagram, the good agreement obtained with the present model gives a good confidence in the description of the thermodynamic behavior of the $LiF-BaF_2-ZrF_4$ system (Fig. 10). Fifteen ternary invariant equilibria are suggested with the present model. The lowest ternary eutectic was found at $T = 589.1$

K and $X_{LiF} = 0.369$, $X_{BaF_2} = 0.247$ and $X_{ZrF_4} = 0.384$. They are listed in Table 9.

Another element of comparison can be found in the thesis of Mahmoud (page 81) [52], that includes an isotherm of this ternary system at 1173 K. The same isothermal projection, calculated in Fig. 11, is in good agreement with this work [52], with the presence of stable solid phases in equilibrium with the liquid at 1173 K at high BaF_2 and ZrF_4 contents. Overall, the agreement on the mixing enthalpies and on this isotherm give us good confidence in the accuracy of the ternary phase diagram presented here.

Based on the model, a calculation of the isothermal projection at 873 K, defined as the minimum operating temperature of the MSR [72], was carried out. As shown in Fig. 12, some crystalline phases are stable in a large compositional area of the phase diagram at this temperature. Since the MSR fuel is not made exclusively of LiF, but of e.g. a $LiF-UF_4-PuF_3/UF_3$ mixture, the more complex equilibria in the fuel-BaF_2-ZrF_4 system should be considered to assess if precipitation of solid phases could occur under operating conditions. This work provides the basis for such calculations.

5. Conclusions

Combining experimentally collected phase diagram data and literature sources on phase diagrams and mixing enthalpy data, thermodynamic models for the binary $LiF-BaF_2$, $LiF-ZrF_4$ and BaF_2-ZrF_4, and ternary $LiF-BaF_2-ZrF_4$ systems were developed for the first time using the modified quasichemical model in the quadruplet approximation for the liquid solution. A large fraction of the intermediates observed in the
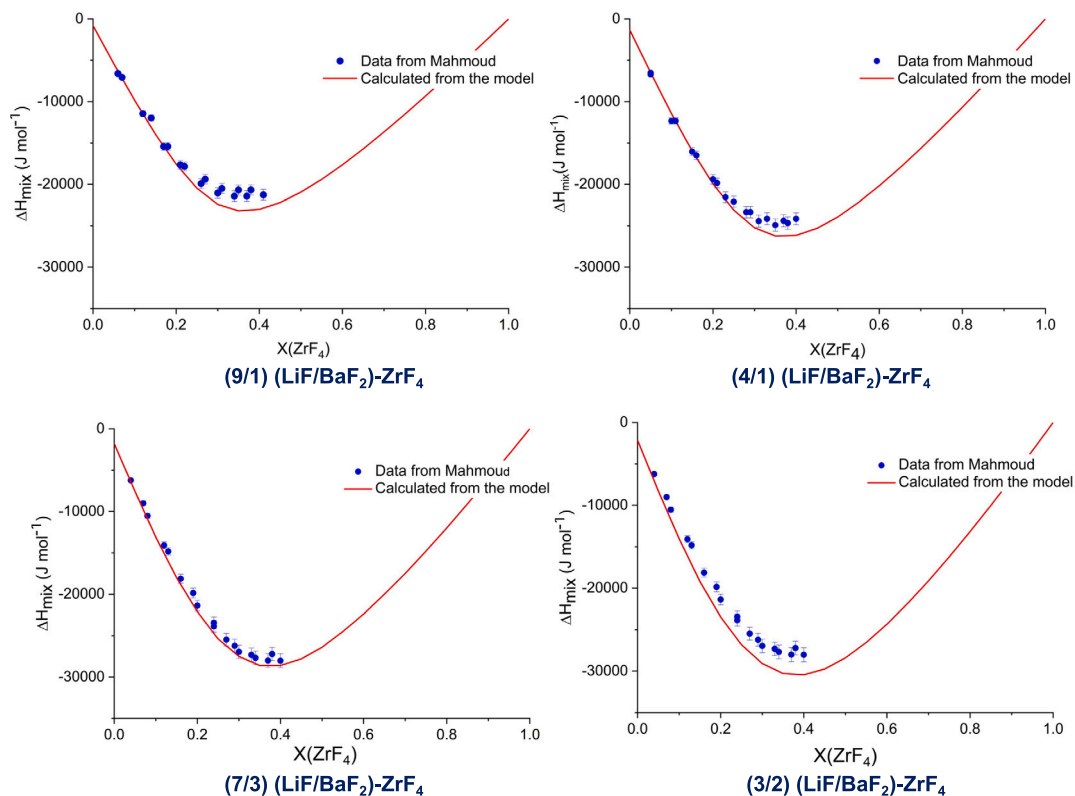
Fig. 8. Mixing enthalpy in the ternary system $LiF-BaF_2-ZrF_4$ for different pseudo-binary sections $((A/B)LiF/BaF_2)-ZrF_4$ (A/B = 9/1; 4/1; 7/3; 3/2) at 1173 K measured by Mahmoud [52] and calculated in this work.
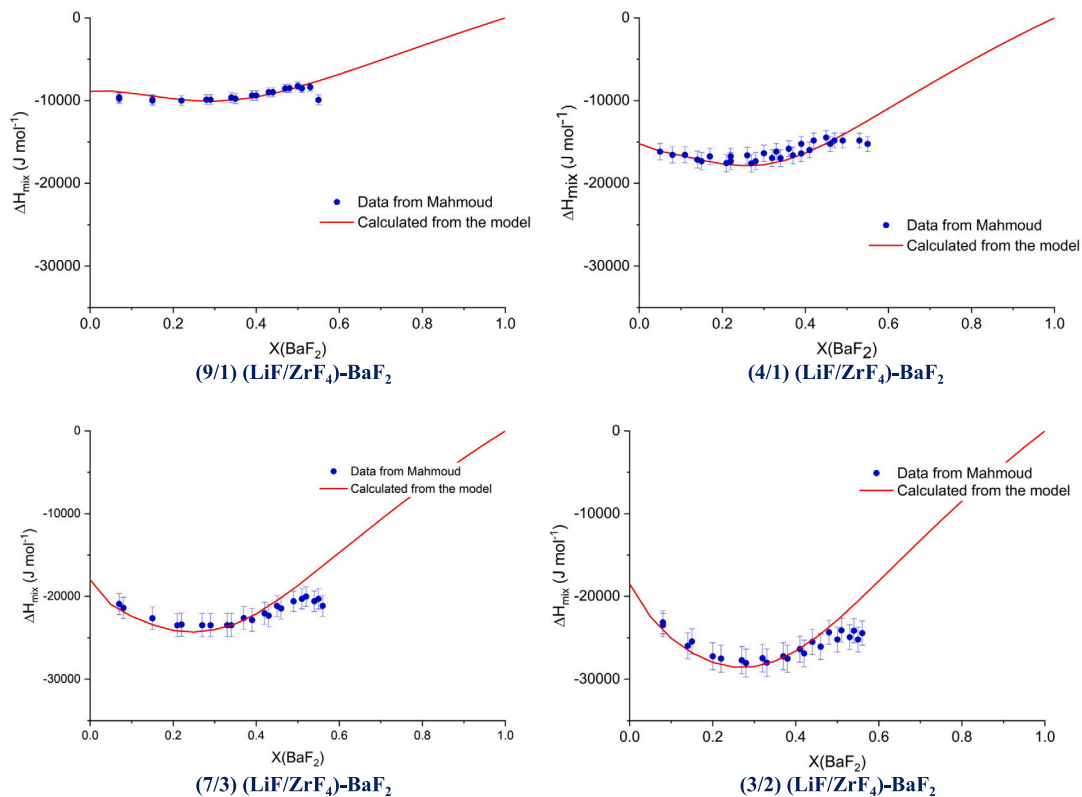

Fig. 9. Mixing enthalpy in the ternary system $LiF-BaF_2-ZrF_4$ for different pseudo-binary sections $((A/B)LiF/ZrF_4)-BaF_2$ (A/B = 9/1; 4/1; 7/3; 3/2) at 1173 K measured by Mahmoud [52] and calculated in this work.
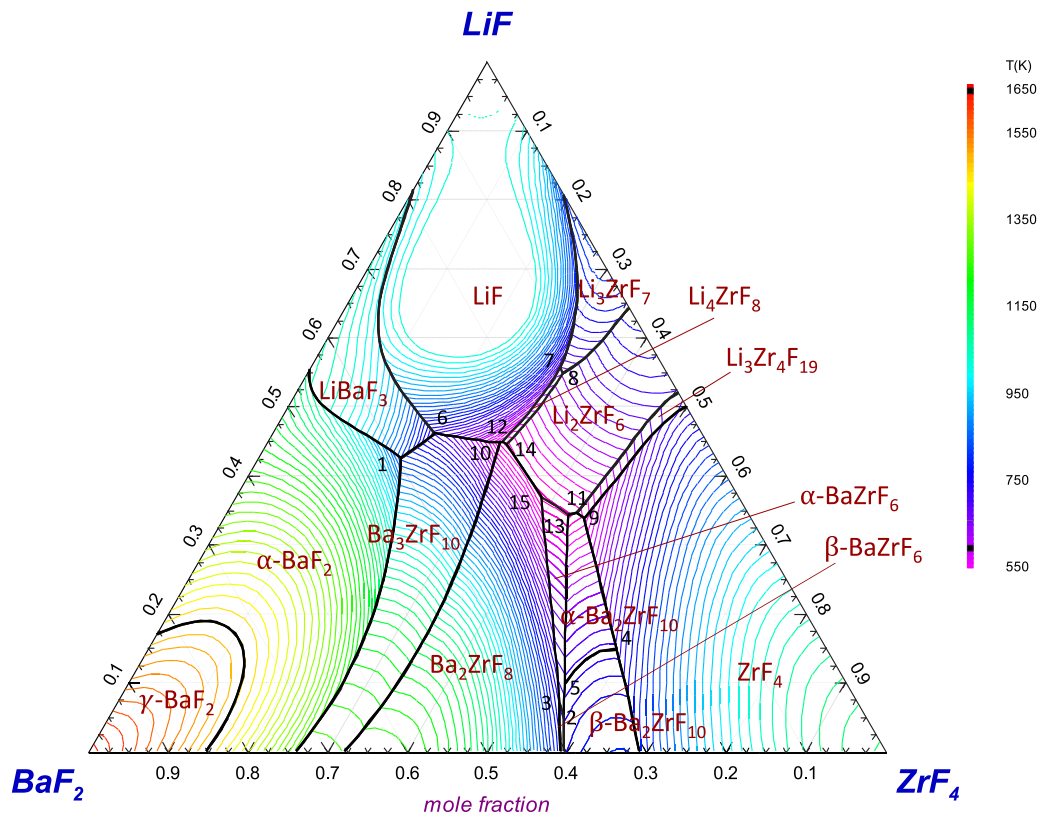
Fig. 10. Liquidus projection of the $LiF-BaF_2-ZrF_4$ system calculated in this work from 550 K to 1650 K with an increment of 15 K. Primary crystallization fields and invariant equilibria are detailed in the figure. The gas phase was excluded in this calculation.
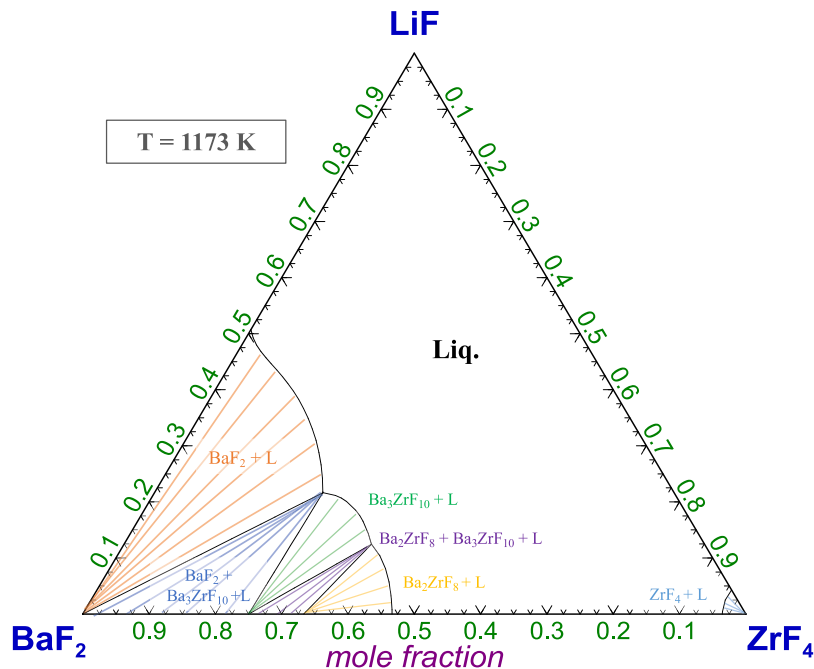

Fig. 11. Isothermal plot of the $LiF-BaF_2-ZrF_4$ system calculated in this work at 1173 K. The calculation were made excluding the gaseous phases. The different stable solid are indicated in the figure.

$LiF-BaF_2-ZrF_4$ system appear to stabilize at the minimum operating temperature of a MSR (873 K). Ba_2ZrF_8 and Ba_3ZrF_{10} were found to be stable solid phases above 1173 K. The possible precipitation of solid phases of LiF, BaF_2 and ZrF_4 in the operating reactor must be taken into consideration for the risk assessment of the MSR. However, the current system only provides equilibria with LiF, which is present in large concentrations in the salt mixture. This forms a basis to study the more complex equilibria with the complete fuel system,
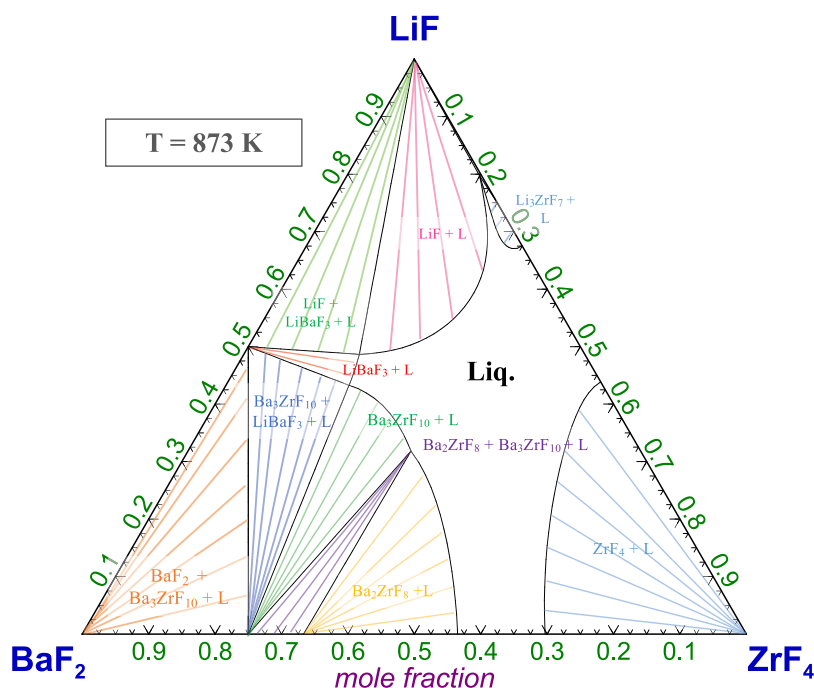
Fig. 12. Isothermal plot of the $LiF-BaF_2-ZrF_4$ system calculated in this work at 873 K. The calculation were made excluding the gaseous phases. The different stable solid phases are indicated in the figure.

Table 9
Invariant equilibria calculated in this work for the system $LiF-BaF_2-ZrF_4$.

N°	X_{LiF}	X_{BaF_2}	X_{ZrF_4}	Invariant equilibria	Transition	T (K)
1	0.425	0.395	0.180	Quasi-peritectic	$L + \alpha\text{-}BaF_2 = Ba_3ZrF_{10} + LiBaF_3$	890.3
2	0.071	0.374	0.555	Phase transition	$\alpha\text{-}BaZrF_6 = \beta\text{-}BaZrF_6$	817.15
3	0.051	0.378	0.571	Phase transition	$\alpha\text{-}BaZrF_6 = \beta\text{-}BaZrF_6$	817.15
4	0.148	0.263	0.589	Phase transition	$\alpha\text{-}BaZr_2F_{10} = \beta\text{-}BaZr_2F_{10}$	796.15
5	0.098	0.353	0.548	Phase transition	$\alpha\text{-}BaZr_2F_{10} = \beta\text{-}BaZr_2F_{10}$	796.15
6	0.461	0.335	0.204	Quasi-peritectic	$L + Ba_3ZrF_{10} = LiBaF_3 + LiF$	788.9
7	0.557	0.129	0.314	Peritectic	$L + Li_3ZrF_7 + LiF = Li_4ZrF_8$	743.0
8	0.548	0.131	0.321	Quasi-peritectic	$L + Li_3ZrF_7 = Li_2ZrF_6 + Li_4ZrF_8$	731.9
9	0.339	0.208	0.453	Quasi-peritectic	$L + ZrF_4 = \alpha\text{-}BaZr_2F_{10} + Li_3Zr_4F_{19}$	615.2
10	0.448	0.259	0.293	Quasi-peritectic	$L + Ba_3ZrF_{10} = Ba_2ZrF_8 + LiF$	602.9
11	0.346	0.214	0.440	Quasi-peritectic	$L + Li_2ZrF_6 = \alpha\text{-}BaZr_2F_{10} + Li_3Zr_4F_{19}$	599.8
12	0.449	0.256	0.295	Quasi-peritectic	$L + Ba_2ZrF_8 = Li_4ZrF_8 + LiF$	595.2
13	0.344	0.226	0.430	Quasi-peritectic	$L + Li_2ZrF_6 = \alpha\text{-}BaZr_2F_{10} + \alpha\text{-}BaZrF_6$	591.3
14	0.445	0.252	0.303	Quasi-peritectic	$L + Ba_2ZrF_8 = Li_4ZrF_8 + Li_2ZrF_6$	590.4
15	0.369	0.247	0.384	Eutectic	$Ba_2ZrF_8 + \alpha\text{-}BaZrF_6 + Li_2ZrF_6 = L$	589.1

e.g. $LiF-ThF_4-UF_4/UF_3$, that should be considered for a more accurate analysis. The volatility of ZrF_4 is in particular a factor to be taken into account for gaseous releases in an accidental scenario.

CRediT authorship contribution statement

Thomas Dumaire: Writing – review & editing, Writing – original draft, Visualization, Methodology, Investigation, Formal analysis, Data curation, Conceptualization. **Luuk Groot:** Methodology, Investigation, Formal analysis, Data curation. **Nynke M. Schakenraad:** Methodology, Investigation, Formal analysis, Data curation. **Ondrej Beneš:** Writing – review & editing, Supervision, Methodology. **Rudy J.M. Konings:** Writing – review & editing, Supervision. **Anna L. Smith:** Writing – review & editing, Supervision, Project administration, Methodology, Funding acquisition, Conceptualization.

Declaration of competing interest

The authors declare the following financial interests/personal relationships which may be considered as potential competing interests:

Thomas Dumaire reports financial support was provided by Euratom Research and Training Programme. If there are other authors, they declare that they have no known competing financial interests or personal relationships that could have appeared to influence the work reported in this paper.

Data availability

Data will be made available on request.

Acknowledgments

References

[1] J.E. Kelly, Generation IV International Forum: A decade of progress through international cooperation, Prog. Nucl. Energy 77 (2014) 240–246, http://dx.doi.org/10.1016/j.pnucene.2014.02.010.

[2] J. Serp, M. Allibert, O. Beneš, S. Delpech, O. Feynberg, V. Ghetta, D. Heuer, D. Holcomb, V. Ignatiev, J.L. Kloosterman, L. Luzzi, E. Merle-Lucotte, J. Uhlíř, R. Yoshioka, D. Zhimin, The molten salt reactor (MSR) in generation IV: Overview and perspectives, Prog. Nucl. Energy 77 (2014) 308–319, http://dx.doi.org/10.1016/j.pnucene.2014.02.014.

[3] O. Beneš, P. Souček, Molten salt reactor fuels, in: Advances in Nuclear Fuel Chemistry, Elsevier, Amsterdam, 2020, pp. 249–271, http://dx.doi.org/10.1016/b978-0-08-102571-0.00007-0.

[4] A. Tosolin, P. Souček, O. Beneš, J.-F. Vigier, L. Luzzi, R.J.M. Konings, Synthesis of plutonium trifluoride by hydro-fluorination and novel thermodynamic data for the PuF$_3$-LiF system, J. Nucl. Mater. 503 (2018) 171–177, http://dx.doi.org/10.1016/j.jnucmat.2018.02.037.

[5] O. Beneš, R.J.M. Konings, Molten Salt Reactor Fuel and Coolant, in: Comprehensive Nuclear Materials, Elsevier, Amsterdam, 2012, pp. 359–389, http://dx.doi.org/10.1016/b978-0-08-056033-5.00062-8.

[6] R.J. Kedl, Migration of a Class of Fission Products (Noble Metals) in the Molten-Salt Reactor Experiment, Oak Ridge National Lab., 1972, http://dx.doi.org/10.2172/4471292, ORNL–TM–2884.

[7] B. Hombourger, J. Křepel, A. Pautz, Breed-and-burn fuel cycle in molten salt reactors, EPJ Nucl. Sci. Technol. 5 (2019) 15, http://dx.doi.org/10.1051/epjn/2019026.

[8] E. Capelli, O. Beneš, R.J.M. Konings, Thermodynamic assessment of the LiF–ThF$_4$–PuF$_3$–UF$_4$ system, J. Nucl. Mater. 462 (2015) 43–53, http://dx.doi.org/10.1016/j.jnucmat.2015.03.042.

[9] J.A. Ocádiz Flores, A.E. Gheribi, J. Vlieland, K. Dardenne, J. Rothe, R.J.M. Konings, A.L. Smith, New insights and coupled modelling of the structural and thermodynamic properties of the LiF-UF$_4$ system, J. Mol. Liq. 331 (2021) 115820, http://dx.doi.org/10.1016/j.molliq.2021.115820.

[10] E. Capelli, O. Beneš, R.J.M. Konings, Thermodynamics of soluble fission products cesium and iodine in the Molten Salt Reactor, J. Nucl. Mater. 501 (2018) 238–252, http://dx.doi.org/10.1016/j.jnucmat.2018.01.024.

[11] J.A. Ocadiz-Flores, E. Capelli, P.E. Raison, R.J.M. Konings, A.L. Smith, Thermodynamic assessment of the LiF-NiF$_2$, NaF-NiF$_2$ and KF-NiF$_2$ systems, J. Chem. Thermodyn. 121 (2018) 17–26, http://dx.doi.org/10.1016/j.jct.2018.01.023.

[12] T. Dumaire, R.J.M. Konings, A.L. Smith, Thermodynamic assessment of the AF–CrF$_3$ (A=Li, Na, K) and CrF$_2$–CrF$_3$ systems, Thermo 1 (2021) 205–219, http://dx.doi.org/10.3390/thermo1020014.

[13] O. Beneš, R.J.M. Konings, Molten salt reactor fuel and coolant, in: R.J.M. Konings, R.E. Stoller (Eds.), Comprehensive Nuclear Materials 2nd Edition, Elsevier, Amsterdam, 2020, pp. 609–644, http://dx.doi.org/10.1016/b978-0-12-803581-8.11790-4.

[14] E.L. Compere, E.G. Bohlmann, S.S. Kirslis, F.F. Blankenship, W.R. Grimes, Fission product behavior in the Molten Salt Reactor Experiment, Office of Scientific and Technical Information (OSTI), Oak Ridge National Laboratory, 1975, http://dx.doi.org/10.2172/4077644, ORNL-4865.

[15] M. Perez, E. van Deventer, M. Akashi, B. Amzal, L. Anspaugh, A. Auvinen, N. Gent, P. Jacob, D. Laurier, C. Miller, O. Niwa, R. Shore, R. Wakeford, L. Walsh, W. Zhang, Health risk assessment from the nuclear accident after the 2011 great east Japan earthquake and tsunami, World Health Organ. Rep. (2013).

[16] A.K. Mishra, N. Garg, K.V. Shanavas, S.N. Achary, A.K. Tyagi, S.M. Sharma, High pressure structural stability of BaLiF$_3$, J. Appl. Phys. 110 (12) (2011) 123505, http://dx.doi.org/10.1063/1.3670036.

[17] L.B. McCusker, R.B. Von Dreele, D.E. Cox, D. Louër, P. Scardi, Rietveld refinement guidelines, J. Appl. Crystallogr. 32 (1) (1999) 36–50, http://dx.doi.org/10.1107/s0021889898009856.

[18] J. Rodriguez-Carvajal, Recent advances in magnetic structure determination by neutron powder diffraction, Physica B 192 (1–2) (1993) 55–69.

[19] W.J. Boettinger, U.R. Kattner, K.-W. Moon, J.H. Perepezko, in: National Institute of Standards and Technology (Ed.), NIST Recommened Practice Guide: DTA and Heat-Flux DSC Measurements of Alloy Melting and Freezing, U.S. Government Printing Office, Washington, DC, 2006, http://dx.doi.org/10.6028/nbs.sp.960-15.

[20] O. Beneš, R.J. Konings, S. Wurzer, M. Sierig, A. Dockendorf, A DSC study of the NaNO$_3$–KNO$_3$ system using an innovative encapsulation technique, Thermochim. Acta 509 (1–2) (2010) 62–66, http://dx.doi.org/10.1016/j.tca.2010.06.003.

[21] C.W. Bale, E. Bélisle, P. Chartrand, S.A. Decterov, G. Eriksson, A.E. Gheribi, K. Hack, I.-H. Jung, Y.-B. Kang, J. Melançon, A.D. Pelton, S. Petersen, C. Robelin, J. Sangster, P. Spencer, M.-A. van Ende, FactSage thermochemical software and databases, 2010–2016, CALPHAD 54 (2016) 35–53, http://dx.doi.org/10.1016/j.calphad.2016.05.002.

[22] U.R. Kattner, H.J. Seifert, H.L. Lukas, Editorial: Integrated computational materials engineering, CALPHAD, CALPHAD, Comput. Coupling Phase Diagr. Thermochem. 34 (2010) 385–386, http://dx.doi.org/10.1016/j.calphad.2010.10.005.

[23] Y.A. Chang, S. Chen, F. Zhang, X. Yan, F. Xie, R. Schmid-Fetzer, W.A. Oates, Phase diagram calculation: past, present and future, Prog. Mater. Sci. 49 (3–4) (2004) 313–345, http://dx.doi.org/10.1016/s0079-6425(03)00025-2.

[24] A.G. Bergman, E.I. Banashek, Ternary systems of fluoride and chloride sodium and barium, Izvestija Sekt. Fiziko-chimiceskogo Anal. 22 (1953) 196–206.

[25] A.I. Agulanskii, V.A. Bessonova, Fusion in salt mixtures containing lithium, barium and lanthanum fluorides, Russ. J. Inorgan. Chem. 27 (4) (1982) 1029–1032.

[26] K.C. Hong, O.J. Kleppa, Enthalpies of mixing in some binary liquid alkali fluoride mixtures, J. Chem. Thermodyn. 8 (1976) 31–36, http://dx.doi.org/10.1016/0021-9614(76)90147-6.

[27] R.E. Thoma, H. Insley, H.A. Friedman, G.M. Hebert, Condensed system LiF-NaF-ZrF$_4$ phase equilibria and crystallographic data, J. Chem. Eng. Data 10 (3) (1965) 219–230, http://dx.doi.org/10.1021/je60026a004.

[28] G. Hatem, M. Gaune-Escard, A. Hoch, Experimental thermodynamics and phase equilibria estimation in Zr-fluoride glasses, J. Non-Cryst. Solids 161 (1993) 91–97, http://dx.doi.org/10.1016/0022-3093(93)90676-o.

[29] T. Grande, S. Aasland, S. Julsrud, Phase equilibria in the glass-forming system ZrF$_4$-BaF$_2$, J. Non-Cryst. Solids 140 (1992) 73–76, http://dx.doi.org/10.1016/s0022-3093(05)80744-6.

[30] G. Hatem, K. Mahmoud, M. Gaune-Escard, Les systemes ternaires fondus ZrF$_4$-BaF$_2$-MF: determination calorimétrique de l'enthalpie d'excès. Partie I. M=Na, Thermochim. Acta 1991 (1991) 91–106, http://dx.doi.org/10.1002/chin.199138016.

[31] O. Beneš, R.J.M. Konings, Thermodynamic calculations of molten-salt reactor fuel systems, in: H.G. Frederic Lantelme (Ed.), Molten Salts Chemistry - From Lab To Applications, Elsevier, Amsterdam, 2013, pp. 49–78, http://dx.doi.org/10.1016/b978-0-12-398538-5.00004-4.

[32] Joint Research Centre - European Commission, in: EU Science Hub (Ed.), Joint Research Centre Molten Salt Database - JRCMSD, 2024, https://joint-research-centre.ec.europa.eu/joint-research-centre-molten-salt-database-jrcmsd_en. (Accessed 05 February 2024).

[33] M.W. Chase Jr., National Information Standards Organization (US), NIST-JANAF Thermochemical Tables, fourth ed., American Intitute of Physics, New York, 1998.

[34] I. Ansara, B. Sundman, The Scientific Group Thermodata Europe (SGTE), Computer Handling Determination of data, Publishing house: Elsevier Science Pub. Co. Amsterdam, Amsterdam, 1987, pp. 154–158.

[35] J. Leitner, P. Voňka, D. Sedmidubský, P. Svoboda, Application of Neumann–Kopp rule for the estimation of heat capacity of mixed oxides, Thermochim. Acta 497 (1–2) (2010) 7–13, http://dx.doi.org/10.1016/j.tca.2009.08.002.

[36] D. Wiedemann, E.M. Heppke, A. Franz, And yet it moves: A high-temperature neutron diffraction study of ion diffusion in the inverse perovskites BaLiX_3 (X=F, H, D), Eur. J. Inorg. Chem. 2019 (48) (2019) 5085–5088, http://dx.doi.org/10.1002/ejic.201901232.

[37] G.D. Brunton, Li$_2$ZrF$_6$, Acta Crystallogr. B 29 (1973) 2294–2296.

[38] P. Dugat, M. El-Ghozzi, J. Metin, D. Avignant, Crystal structure of Li$_4$ZrF$_8$ and Li$_3$Zr$_4$F$_{19}$ and reinvestigation of the LiF-ZrF$_4$ phase diagram, J. Solid State Chem. 120 (1) (1995) 187–196, http://dx.doi.org/10.1006/jssc.1995.1396.

[39] J.-P. Laval, B. Frit, Une nouvelle structure ordonnée dérivée de la fluorine : Pb$_3$ZrF$_{10}$, Mater. Res. Bull. 15 (1) (1980) 45–52, http://dx.doi.org/10.1016/0025-5408(80)90158-0.

[40] A.L. Bail, J.-P. Laval, Synthesis and crystal structure of α-Ba$_2$ZrF$_8$ and Pb$_2$ZrF$_8$ determined ab initio from synchrotron and neutron powder diffraction data, Eur. J. Inorg. Solid State Chem. 35 (4–5) (1998) 357–372, http://dx.doi.org/10.1016/s0992-4361(98)80432-3.

[41] J.-P. Laval, R. Papiernik, B. Frit, BaZrF$_6$ α: une structure à anion complexe [Zr$_2$F$_{12}$]$^{4-}$, Acta Crystallogr. B 34 (4) (1978) 1070–1074, http://dx.doi.org/10.1107/s056774087800494x.

[42] B. Mehlhorn, R. Hoppe, Neue Hexafluorozirkonate(IV): BaZrF$_6$, PbZrF$_6$, EuZrF$_6$, SrZrF$_6$, Z. Anorg. Allg. Chem. 425 (2) (1976) 180–188, http://dx.doi.org/10.1002/zaac.19764250213.

[43] J.-P. Laval, The low-temperature barium fluoridozirconate variety α-BaZr$_2$F$_{10}$, Acta Crystallogr. C 75 (11) (2019) 1482–1487, http://dx.doi.org/10.1107/s205322961901297x.

[44] J.-P. Laval, B. Frit, J. Lucas, Crystal structure of the βBaZr$_2$F$_{10}$ compound. Relations with the ReO$_3$-type and the fluorozirconate glasses, J. Solid State Chem. 72 (2) (1988) 181–192, http://dx.doi.org/10.1016/0022-4596(88)90021-7.

[45] C. Bale, P. Chartrand, S. Degterov, G. Eriksson, K. Hack, R. Ben Mahfoud, J. Melançon, A. Pelton, S. Petersen, FactSage thermochemical software and databases, CALPHAD 26 (2) (2002) 189–228, http://dx.doi.org/10.1016/s0364-5916(02)00035-4.

[46] I.D. Ratnikova, Y.M. Korenev, P.P. Fedorov, B.P. Sobolev, Phase diagrams of BaF$_2$ - RF$_4$ systems (R=Zr, Hf), J. Inorg. Chem. 42 (2) (1997) 246–251.

[47] A.A. Babitsyna, T.A. Emelyanova, A.N. Chernov, Investigation of systems MF$_2$-ZrF$_4$ (M-Ba, Pb, Zn, Cd) (Russian), J. Inorg. Chem. 34 (12) (1989).

[48] A.A. Babitsyna, T.A. Emelyanova, E.G. Zhukov, Phase relations in the PbF$_2$-BaF$_2$-ZrF$_4$ system, Inorg. Mater. 42 (9) (2006) 1020–1022, http://dx.doi.org/10.1134/s0020168506090160.

[49] A.D. Pelton, S. Degterov, G. Eriksson, C. Robelin, Y. Dessureault, The modified quasichemical model I—binary solutions, Metall. Mater. Trans. B 31 (4) (2000) 651–659, http://dx.doi.org/10.1007/s11663-000-0103-2.

[50] O. Beneš, M. Beilmann, R.J.M. Konings, Thermodynamic assessment of the LiF–NaF–ThF$_4$–UF$_4$ system, J. Nucl. Mater. 405 (2) (2010) 186–198, http://dx.doi.org/10.1016/j.jnucmat.2010.08.017.

[51] A.D. Pelton, P. Chartrand, The modified quasi-chemical model: Part II. Multicomponent solutions, Metall. Mater. Trans. A 32A (6) (2001) 1355–1360, http://dx.doi.org/10.1007/s11661-001-0226-3.

[52] K. Mahmoud, Mélanges fondus à base de fluorure de zirconium : Etude experimentale à haute température et modélisation des fonctions thermodynamiques (Ph.D. thesis), Aix Marseille University, 1989.

[53] K.A. Sense, R.W. Stone, Vapor pressures and molecular composition of vapors of the RbF-ThF$_4$ and LiF-ZrF$_4$ systems, J. Phys. Chem. 62 (1958) 1411–1418.

[54] I. Nuta, C. Chatillon, H. Collas, L. Artaud, V. Guetta, D. Heuer, Vapor pressure measurements of LiF-ZrF$_4$ for Molten Salt Fast Reactor, CALPHAD 51 (2015) 367, http://dx.doi.org/10.1016/j.calphad.2015.01.077.

[55] M.A. Boukhalova, Ternary systems of the fluorides and chlorides sodium and strontium, Izvestija Sekt. Fiziko-chimiceskogo Anal. (Trans. Knowl. Sect. Phys. Chem. Anal.) 26 (1955) 138–146.

[56] K. Taniuchi, T. Kanai, A. Inoue, Electrical conductivities of molten salts of some binary fluoride systems containing lithium fluoride, J. Japan Inst. Light Met. 26 (111) (1976).

[57] K.C. Hong, O.J. Kleppa, Thermochemistry of the liquid mixtures of the alkaline earth fluorides with alkali fluorides, J. Phys. Chem. 82 (14) (1978) 1596–1603, http://dx.doi.org/10.1021/j100503a005.

[58] R.J.M. Konings, D. Hildenbrand, The vapor pressure, infrared spectrum, and thermodynamic properties of ZrF$_4$(g), J. Chem. Thermodyn. 26 (2) (1994) 155–163, http://dx.doi.org/10.1006/jcht.1994.1033.

[59] Y. Luo, J. Dai, Q. Dou, H. Fu, Q. Li, Influence of free F$^-$ anions on evaporation behavior of molten salts containing ZrF$_4$, J. Nucl. Mater. 561 (2022) 153550, http://dx.doi.org/10.1016/j.jnucmat.2022.153550.

[60] C.J. Barton, H.A. Friedman, W.R. Grimes, H. Insley, R.E. Moore, R.E. Thoma, Phase equilibria in the alkali fluoride-uranium tetrafluoride fused salt systems: I, the systems LiF-UF$_4$ and NaF-UF$_4$, J. Am. Ceram. Soc. 41 (2) (1958) 63–69, http://dx.doi.org/10.1111/j.1151-2916.1958.tb13520.x.

[61] C.J. Barton, W.R. Grimes, H. Insley, R.E. Moore, R.E. Thoma, Phase equilibria in the systems NaF-ZrF$_4$, UF$_4$-ZrF$_4$ and NaF-ZrF$_4$-UF$_4$, J. Phys. Chem. 62 (6) (1958) 665–676.

[62] H.A. Friedman, G.M. Hebert, R.E. Thoma, Thermal Analysis and Gradient Quenching Apparatus and Techniques for the Investigation of Fused Salt Phase Equilbria, Oak Ridge National Laboratory, 1963, ORNL-3373.

[63] Y.M. Korenev, A.V. Novoselova, K.K. Glinskii, V.V. Shornikov, A study of the LiF-ZrF$_4$ system, Izv. Akad. Nauk SSSR Neorg. Mater. 1 (2) (1964) 201–203.

[64] P.L. Brown, E. Curti, B. Grambow, C. Ekberg, Chemical thermodynamics of zirconium, in: F.J. Mompean, J. Perrone, M. Illemassène (Eds.), in: OECD Nuclear Energy Agency, Data Bank, vol. 8, Elsevier, Amsterdam, 2005.

[65] Junhua Xi, Yanwei Huang, Pressure-induced phase transitions of hydrous zirconium tetrafluoride, Glass Phys. Chem. 45 (2) (2019) 133–137, http://dx.doi.org/10.1134/S1087659619020123.

[66] A.L. Smith, E. Capelli, R.J.M. Konings, A.E. Gheribi, A new approach for coupled modelling of the structural and thermo-physical properties of molten salts. Case of a polymeric liquid LiF-BeF$_2$, J. Mol. Liq. 299 (2020) 112165, http://dx.doi.org/10.1016/j.molliq.2019.112165.

[67] A.L. Smith, Structure-property relationships in actinide containing molten salts – A review: Understanding and modelling the chemistry of nuclear fuel salts, J. Mol. Liq. 360 (2022) 119426, http://dx.doi.org/10.1016/j.molliq.2022.119426.

[68] G. Hatem, F. Tabaries, M. Gaune-Escard, Enthalpies de Formation des Mélanges Liquides ZrF$_4$-MF (M=Li, Na, K, Rb), Thermochim. Acta 149 (1989) 15–26, http://dx.doi.org/10.1016/0040-6031(89)85263-3.

[69] I.-C. Lin, A. Navrotsky, J. Ballato, R.E. Riman, High-temperature calorimetric study of glass-forming fluorozirconates, J. Non-Cryst. Solids 215 (2–3) (1997) 113–124, http://dx.doi.org/10.1016/S0022-3093(97)00081-1.

[70] Y. Gao, J. Guery, C. Jacoboni, ChemInform abstract: Crystal structure determination of LiBaZr$_2$F$_{11}$, ChemInform 24 (8) (1993) http://dx.doi.org/10.1002/chin.199308012.

[71] K. Wang, Development of the modified quasichemical model in the distinguishable-pair approximation for multiple compositions of short-range ordering, J. Mol. Liq. 362 (2022) 119671, http://dx.doi.org/10.1016/j.molliq.2022.119671.

[72] A. Mourogov, P. Bokov, Potentialities of the fast spectrum molten salt reactor concept: REBUS-3700, Energy Convers. Manage. 47 (17) (2006) 2761–2771, http://dx.doi.org/10.1016/j.enconman.2006.02.013.